Article

A Nonlinear Elastic Model for Triaxial Compressive Properties of Artificial Methane-Hydrate-Bearing Sediment Samples

Kuniyuki Miyazaki [1],*, Norio Tenma [2], Kazuo Aoki [2] and Tsutomu Yamaguchi [3]

[1] Institute for Geo-Resources and Environment, National Institute of Advanced Industrial Science and Technology, 1-1-1 Higashi, Tsukuba, Ibaraki 305-8567 Japan

[2] Methane Hydrate Research Center, National Institute of Advanced Industrial Science and Technology, 16-1 Onogawa, Tsukuba, Ibaraki 305-8569 Japan;
E-Mails: tenma-n@aist.go.jp (N.T.); aoki-kazuo@aist.go.jp (K.A.)

[3] Department of Environmental Science, Toho University, 2-2-1 Miyama, Funabashi, Chiba 274-8510 Japan; E-Mail: yamaguchi@env.sci.toho-u.ac.jp

* Author to whom correspondence should be addressed; E-Mail: miyazaki-kuniyuki@aist.go.jp; Tel.: +81-29-861-8753; Fax: +81-29-861-8738.

Abstract: A constitutive model for marine sediments containing natural gas hydrate is essential for the simulation of the geomechanical response to gas extraction from a gas-hydrate reservoir. In this study, the triaxial compressive properties of artificial methane-hydrate-bearing sediment samples reported in an earlier work were analyzed to examine the applicability of a nonlinear elastic constitutive model based on the Duncan-Chang model. The presented model considered the dependences of the mechanical properties on methane hydrate saturation and effective confining pressure. Some parameters were decided depending on the type of sand forming a specimen. The behaviors of lateral strain *versus* axial strain were also formulated as a function of effective confining pressure. The constitutive model presented in this study will provide a basis for an elastic analysis of the geomechanical behaviors of the gas-hydrate reservoir in the future study, although it is currently available to a limited extent.

1. Introduction

Natural gas hydrates are anticipated to be a promising energy resource [1–4]. The mechanical property of a gas hydrate reservoir is considered to be essential for sustainable production, because it will affect the stability of a wellbore or other subsea structures, the occurrence of geohazards and gas productivity [5–8].

A constitutive model for gas-hydrate-bearing sediments is required for the simulation of the geomechanical response to gas extraction from a gas-hydrate reservoir. Laboratory studies are useful for constructing a constitutive model for gas-hydrate-bearing sediments. However, few constitutive model for gas-hydrate-bearing sediments has been published [9], although there have been reports on laboratory studies concerning the triaxial compressive properties of natural and artificial gas-hydrate-bearing sediment samples [10–19].

An elastic constitutive model may be practically useful for the preliminary simulation of the mechanical behavior of a reservoir on the condition that we use it with particular attention to the applicable range. In this study, the application of the Duncan-Chang model, a nonlinear elastic model, to the analysis of the triaxial compressive properties of artificial methane-hydrate-bearing sediment samples reported mainly in an earlier work [19] was examined. The dependences of the mechanical properties on methane hydrate saturation and effective confining pressure were considered.

2. Review of Triaxial Compression Test

The methods and results of triaxial compression test for artificial methane-hydrate-bearing sediments were described in our previous studies [12,14,16–19]. In this section, the test methods and results are briefly described.

2.1. Test Methods

Host specimens were prepared by freezing a cylindrical unsaturated sand specimen. The skeleton of each specimen was formed by Toyoura sand (average particle size $D_{50} = 230 \times 10^{-6}$ m, fine fraction content $F_c = 0.0\%$), No. 7 silica sand ($D_{50} = 205 \times 10^{-6}$ m, $F_c = 1.1\%$) or No. 8 silica sand ($D_{50} = 130 \times 10^{-6}$ m, $F_c = 11.5\%$). These three types of sand contain SiO_2 as a major component. The relative density of each host specimen was over 96%. The average porosities of the host specimens formed by Toyoura sand, No. 7 silica sand and No. 8 silica sand were 37.8%, 38.6% and 41.2%, respectively. The relative density of each host specimen was over 96%. Each host specimen was 50 mm in diameter and 100 mm in length.

The artificial methane-hydrate-bearing sediment samples, which are hereafter referred to as a "hydrate-sand specimen," were prepared from the frozen host sand by the following procedure. First, a cell pressure of 0.5 MPa, 1 MPa, 2 MPa or 3 MPa was applied. Second, the pore air in the specimen was replaced by the methane at 268 K or less. Third, the pore gas pressure was increased to 8 MPa at a rate of approximately 0.7 MPa/min, whereas the cell pressure was increased to 8.5 MPa, 9 MPa, 10 MPa or 11 MPa at the same rate. Forth, the temperature inside the triaxial cell was increased to 278 K. The cell pressure, pore gas pressure and temperature were then kept constant for 24 h during the hydrate formation period. The pore gas pressure was controlled by a pressure-reducing valve

attached to the methane gas cylinder. Finally, water was injected into the specimen to replace the residual gaseous methane in the pores of the specimen. We also prepared "sand specimens," *i.e.*, water-saturated specimens of densely packed sand sediment without hydrate by omitting the methane hydrate formation process from the above-described procedure.

Axial loading was conducted at an axial strain rate of 0.1%/min under a drained condition while maintaining the pore pressure at 8 MPa, the cell pressure at 8.5 MPa, 9 MPa, 10 MPa or 11 MPa and the temperature at 278 K. The methane hydrate existing in the specimen was dissociated by reducing pore pressure after the axial loading. Then, the volume of released methane was measured using a gas flow meter. Assuming that all the released gas have been converted to the hydrate during the axial loading, the initial volume of the methane hydrate formed in the specimen, and thus the methane hydrate saturation S_h, was calculated from the volume of released methane, where S_h is the initial volume percentage of methane hydrate in the pores of the specimen. The methane hydrate saturation S_h of each hydrate-sand specimen used in this study was below 60%.

2.2. Test Results

Figure 1 shows the deviator stress q plotted against the axial strain ε_a and lateral strain ε_l for the sand specimens (a: $S_h = 0\%$) and hydrate-sand specimens (b: $S_h = 27\%–34\%$, c: $S_h = 41\%–45\%$) formed by Toyoura sand under the effective confining pressures σ_3' of 0.5 MPa, 1 MPa, 2 MPa and 3 MPa. In Figure 1, as well as in Figures 2–5, solid lines represent the experimental results reported in the earlier work [19] and broken lines represent the calculated results with the constitutive model which will be described later. Axial/lateral strain was calculated by dividing the axial/lateral displacement measured with the LVDTs using the initial height/diameter of the specimen in this paper. Note that the lateral displacement was measured at the middle height of the specimen. A positive strain denotes compression in this paper. The q increases and the slopes of the q-ε_a and q-ε_l curves decrease until q reaches a peak, and then q gradually decreases. Under a given σ_3', the larger the S_h, the larger the strength (maximum deviator stress) q_f and the initial tangent elastic modulus E_i. For a given S_h, the specimen has a larger q_f and larger E_i and becomes more ductile under a higher σ_3', as in the case of other geological materials.

Figure 2 shows the ε_l plotted against the ε_a for the sand specimens (a: $S_h = 0\%$) and hydrate-sand specimens (b: $S_h = 27\%–34\%$, c: $S_h = 41\%–45\%$) formed by Toyoura sand under the σ_3' of 0.5 MPa, 1 MPa, 2 MPa and 3 MPa. All the ε_l-ε_a curves are concave upward in this graph. A specimen of higher S_h has a tendency to expand further in the lateral direction. It is also found that ε_l tends to decrease with increasing σ_3' at a given ε_a.

Figure 1. Experimental (solid lines) and calculated (broken lines) deviator stress *q versus* axial strain ε_a and lateral strain ε_l for specimens formed by Toyoura sand with methane hydrate saturation S_h of (**a**) 0%; (**b**) 27%–34% and (**c**) 41%–45%. Experimental results are taken from the reference [19].
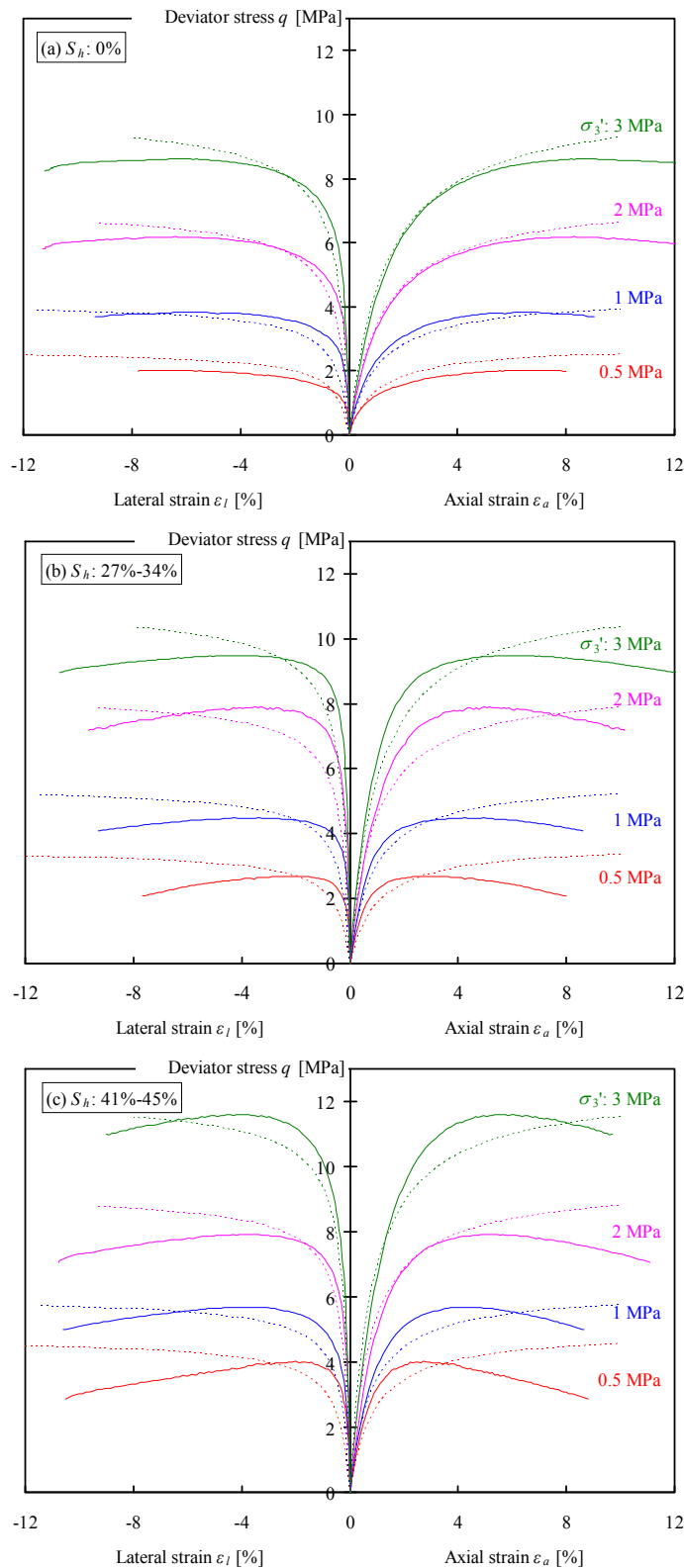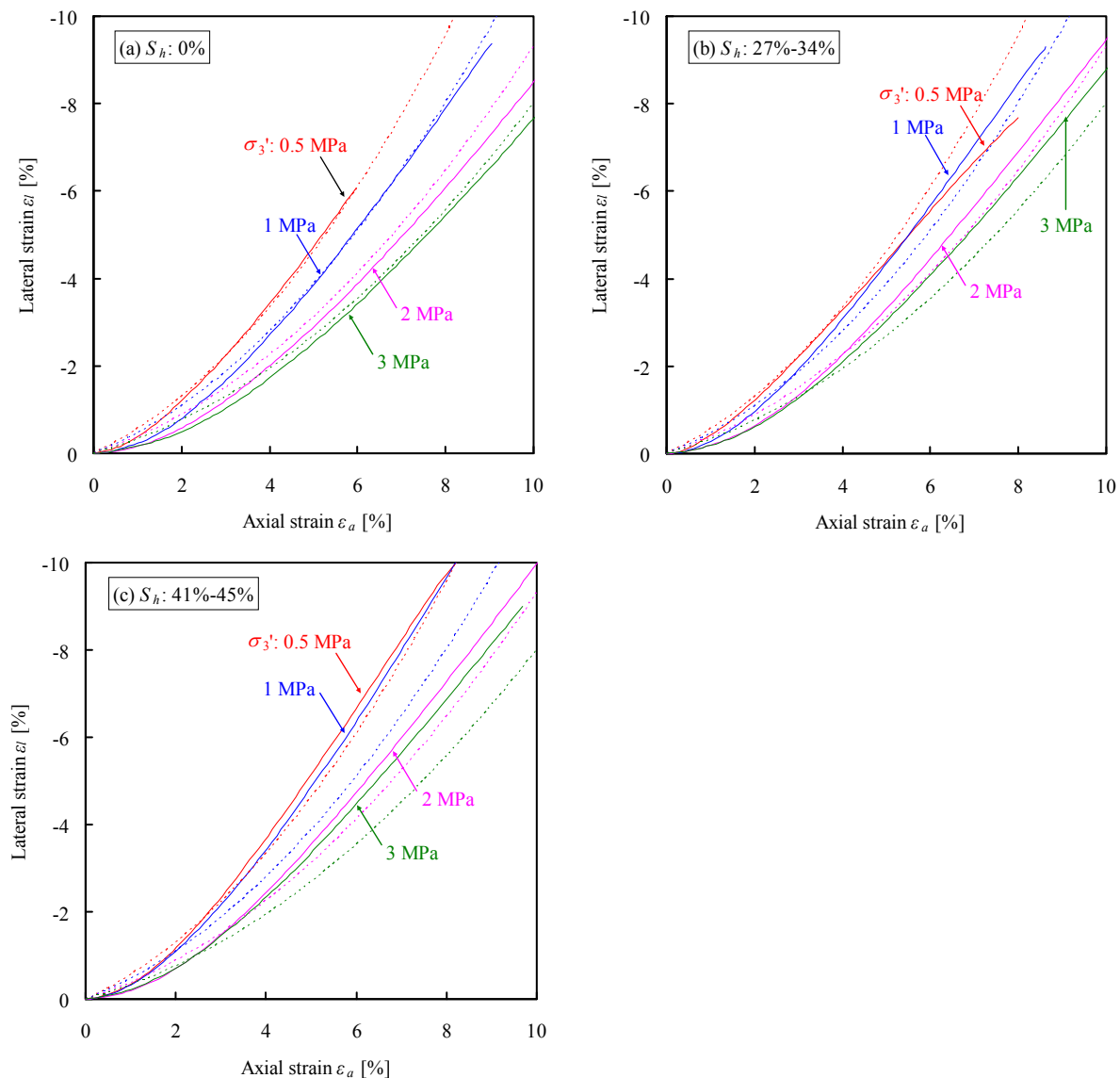
Figure 2. Experimental (solid lines) and calculated (broken lines) lateral strain ε_l *versus* axial strain ε_a for specimens formed by Toyoura sand with methane hydrate saturation S_h of (**a**) 0%; (**b**) 27%–34% and (**c**) 41%–45%. Experimental results are taken from the reference [19].

Figures 3 and 4 show the q-ε_a and q-ε_l curves and the ε_l-ε_a curves, respectively, for the specimens formed by No. 7 silica sand. Figures 5 and 6 show the q-ε_a and q-ε_l curves and the ε_l-ε_a curves, respectively, for the specimens formed by No. 8 silica sand. It is found that the relationships among the q, ε_a and ε_l for the specimens formed by No. 7 and No. 8 silica sand are qualitatively similar to those for the specimens formed by Toyoura sand.

Figure 3. Experimental (solid lines) and calculated (broken lines) deviator stress *q versus* axial strain ε_a and lateral strain ε_l for specimens formed by No. 7 silica sand with methane hydrate saturation S_h of (**a**) 0%; (**b**) 23%–28% and (**c**) 49%. Experimental results are taken from the reference [19].
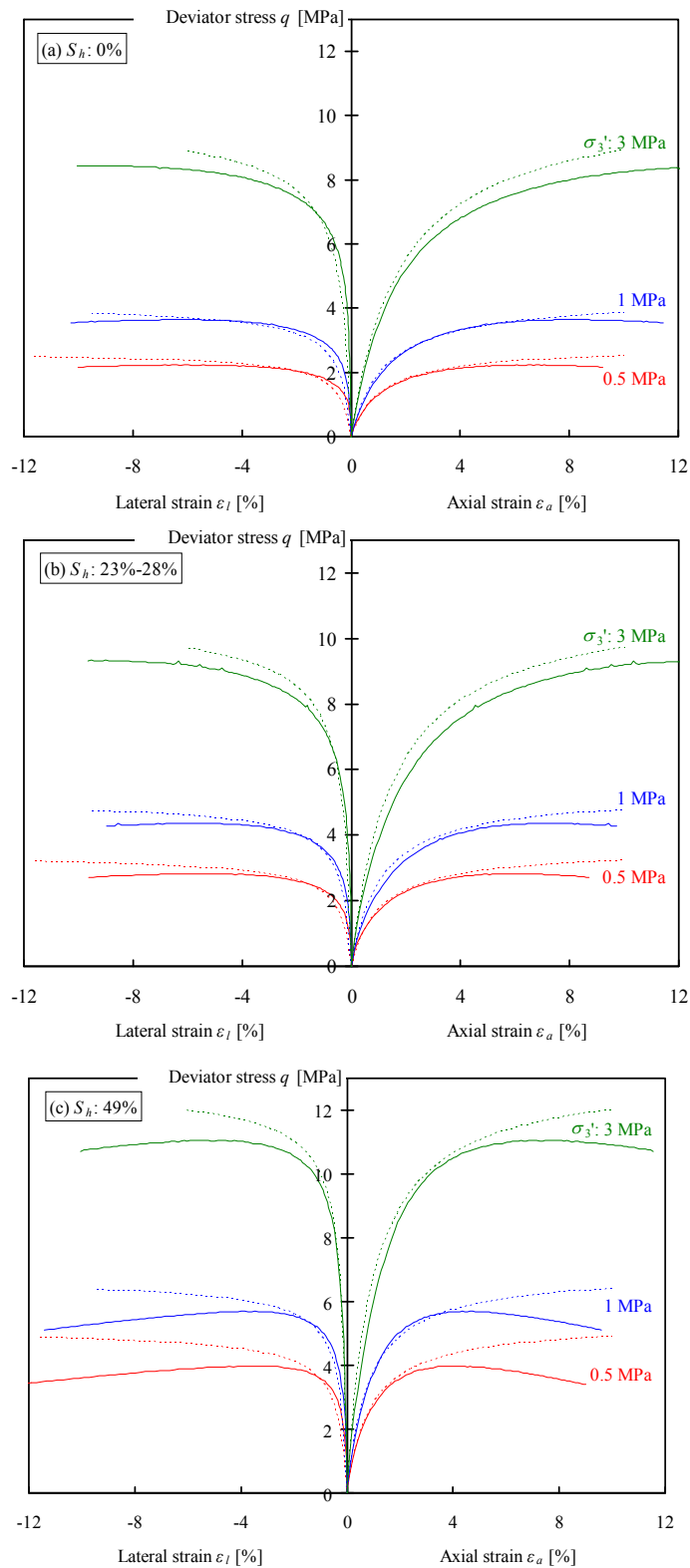
Figure 4. Experimental (solid lines) and calculated (broken lines) lateral strain ε_l *versus* axial strain ε_a for specimens formed by No. 7 silica sand with methane hydrate saturation S_h of (**a**) 0%; (**b**) 23%–28% and (**c**) 49%. Experimental results are taken from the reference [19].
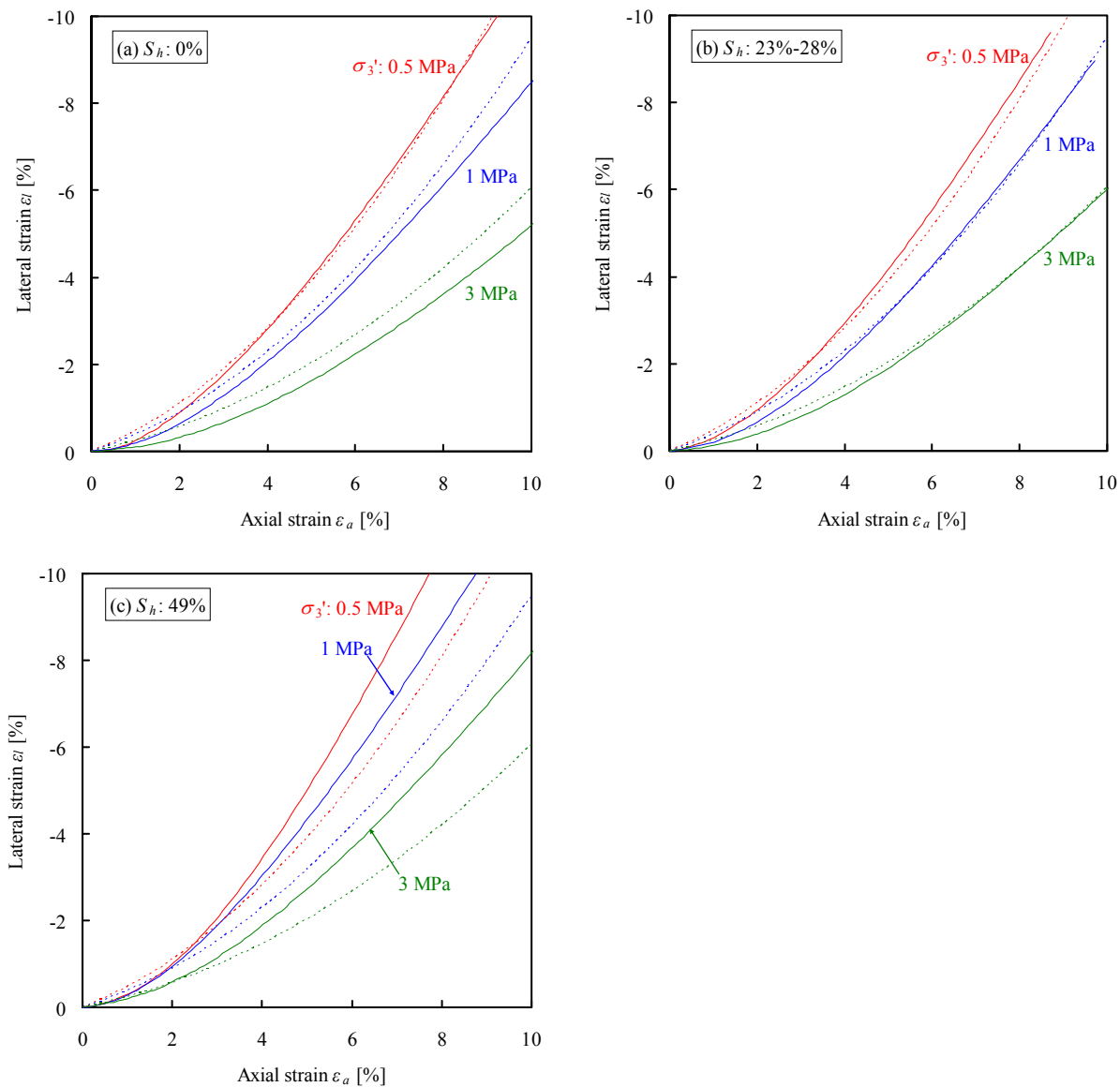
Figure 5. Experimental (solid lines) and calculated (broken lines) deviator stress *q versus* axial strain ε_a and lateral strain ε_l for specimens formed by No. 8 silica sand with methane hydrate saturation S_h of (**a**) 0%; (**b**) 19%–23% and (**c**) 44%–50%. Experimental results are taken from the reference [19].
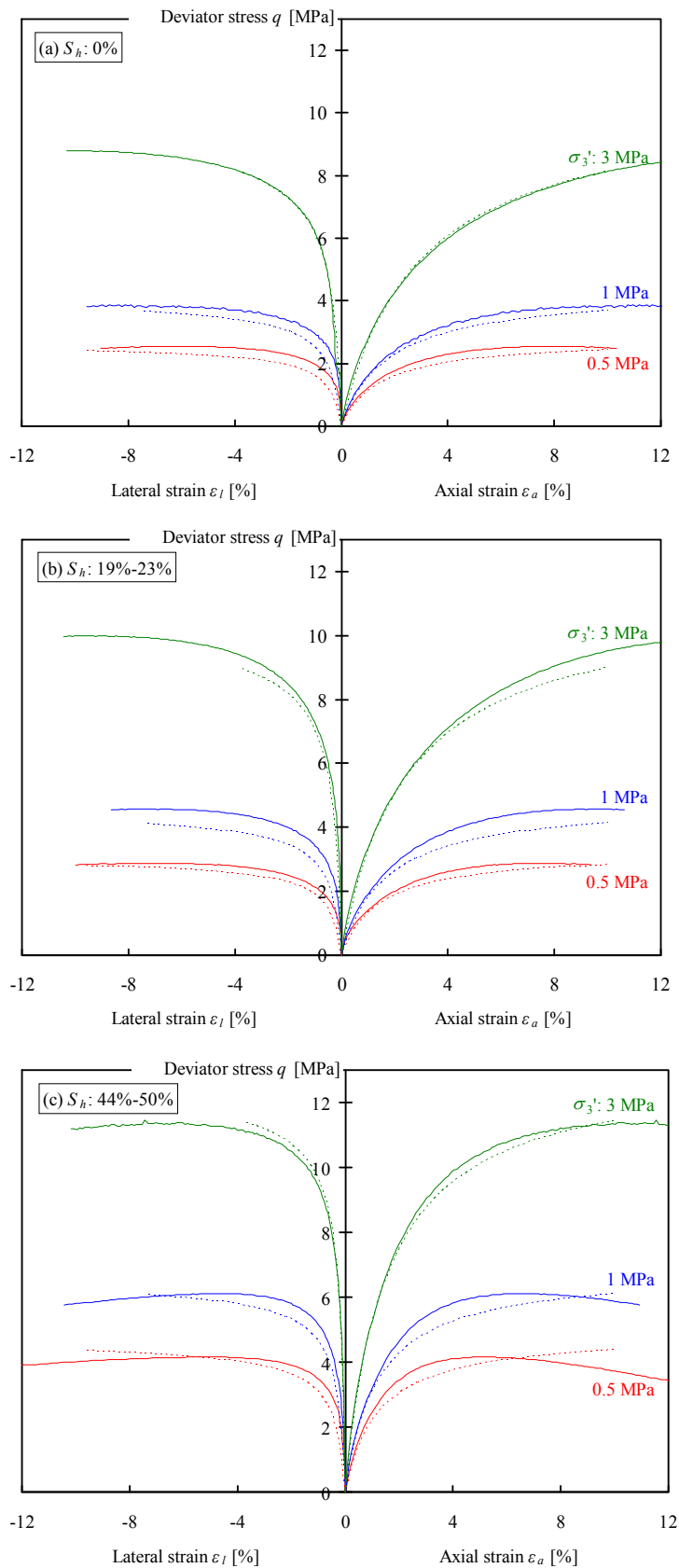
Figure 6. Experimental (solid lines) and calculated (broken lines) lateral strain ε_l *versus* axial strain ε_a for specimens formed by No. 8 silica sand with methane hydrate saturation S_h of (**a**) 0%; (**b**) 19%–23% and (**c**) 44%–50%. Experimental results are taken from the reference [19].
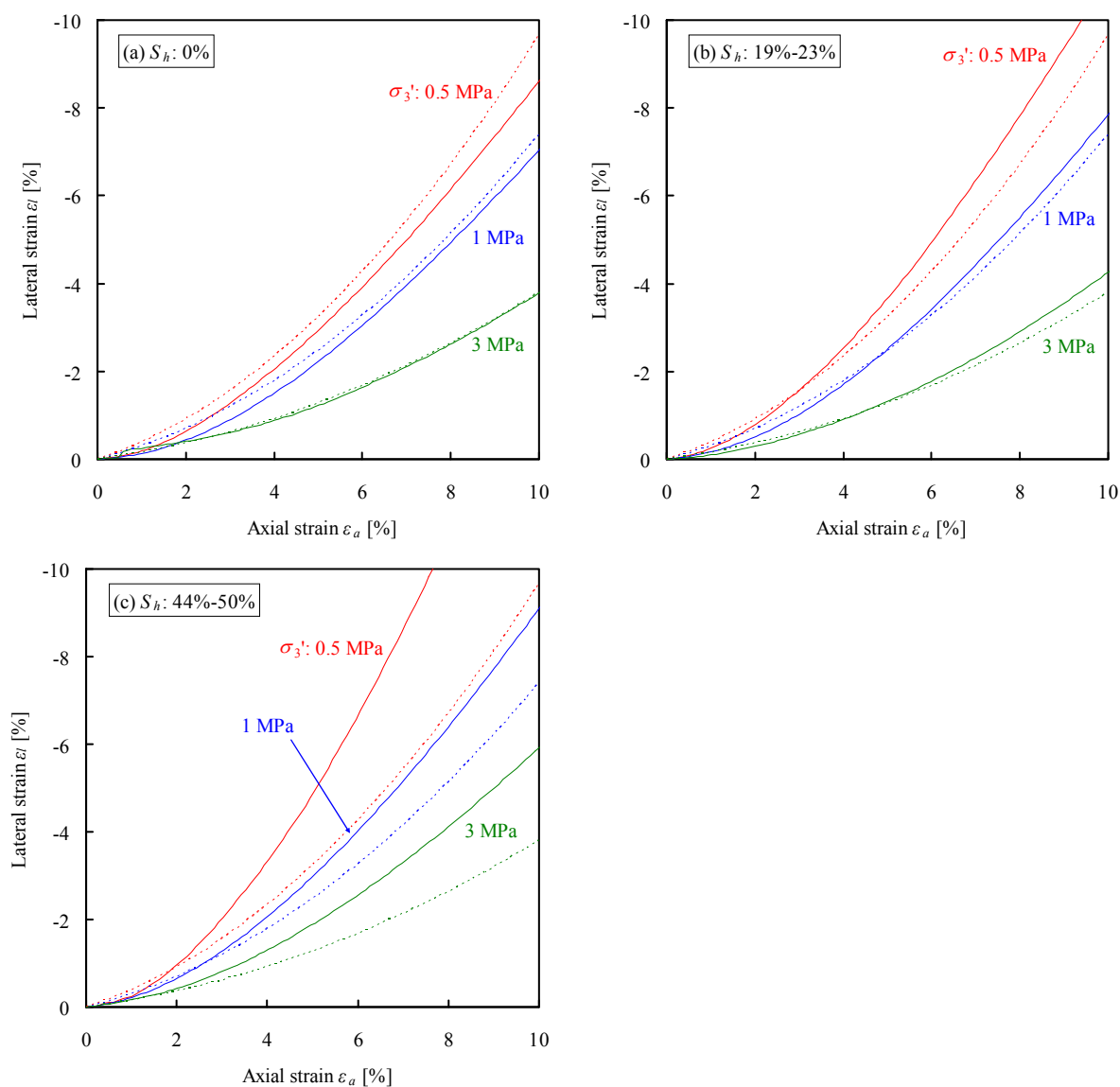

Figure 7 shows the strength q_f plotted against the methane hydrate saturation S_h for the specimens formed by Toyoura sand, No. 7 silica sand and No. 8 silica sand as the skeleton. The strength q_f increases with S_h under each effective confining pressure σ_3'. It can be seen that there is little difference in strength among the three types of sand and hydrate-sand specimens formed by Toyoura sand, No. 7 silica sand and No. 8 silica sand at the same S_h and σ_3'.

Figure 7. Strength q_f *versus* methane hydrate saturation S_h. Experimental results are taken from the reference [19].
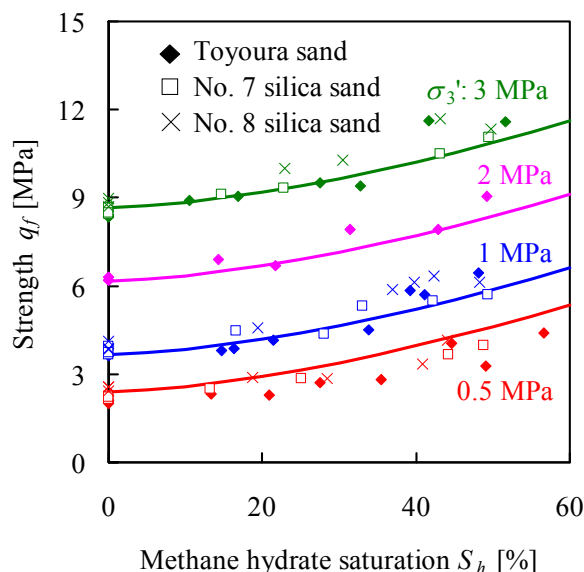
3. Nonlinear Elastic Constitutive Model

3.1. Duncan-Chang Model

Miyazaki *et al.* [20] suggested a possibility of application of Duncan-Chang model to the stress-strain relationships of hydrate-sand specimen formed by Toyoura sand. Duncan and Chang [21] described the following nonlinear elastic constitutive model:

$$q = \frac{\varepsilon_a}{a + b \cdot \varepsilon_a} \tag{1}$$

where *a* and *b* are coefficients related to the initial tangent elastic modulus E_i and the asymptotic value of the deviator stress q_{ult}, as shown by:

$$a = \frac{1}{E_i} \tag{2}$$

$$b = \frac{1}{q_{ult}} \tag{3}$$

Equation (1) can be rewritten as:

$$\frac{\varepsilon_a}{q} = a + b \cdot \varepsilon_a \tag{4}$$

Thus, *a* and *b*, and ultimately E_i and q_{ult}, can be determined by the linear approximation of the experimental (ε_a/q)-ε_a data. In this study, the (ε_a/q)-ε_a data at the stress level (q/q_f) in the range of 70% to 95% were used to determine *a* and *b*, as recommended in Duncan and Chang's study [21].

3.2. Strength

The four curves shown in Figure 7 represent the calculated strengths for the effective confining pressures σ_3' of 0.5 MPa, 1 MPa, 2 MPa and 3 MPa with the following equations as functions of σ_3' and S_h:

$$q_f = \frac{2 \cdot \cos\varphi}{1 - \sin\varphi} c_0 + \alpha \cdot S_h^{\beta} + \frac{2 \cdot \sin\varphi}{1 - \sin\varphi} \sigma_3' \tag{5}$$

$$c_0 = 0.30 \text{ MPa} \tag{6}$$

$$\varphi = 33.8° \tag{7}$$

$$\alpha = 4.64 \times 10^{-3} \tag{8}$$

$$\beta = 1.58 \tag{9}$$

The form of Equation (5) is determined on the basis of the Mohr-Coulomb failure theory and the observation by Masui *et al.* [14] indicating that the cohesion increases with S_h and the internal friction angle φ is almost independent of S_h. The values of the parameters in Equation (5) were determined as Equations (6–9) using all of the experimental data shown in Figure 7.

3.3. Initial Tangent Elastic Modulus

Figure 8 shows E_i, or the inverse of a, plotted against the methane hydrate saturation S_h. It is found that E_i shows an increasing trend with S_h and σ_3', although quite a variation can be seen. Janbu [22] has shown that the relationship between E_i and σ_3' may be expressed as:

$$E_i = K \cdot p_a \cdot \left(\frac{\sigma_3'}{p_a}\right)^n \tag{10}$$

where p_a = atmospheric pressure, K = a modulus number and n = the exponent determining the rate of variation of E_i with σ_3', indicating that E_i is proportional to the *n*-th power of σ_3'. Thus, in this study, it is assumed that E_i can be expressed as a function of S_h and σ_3' as:

$$E_i(S_h, \sigma_3') = e_i(S_h) \cdot \sigma_3'^n \tag{11}$$

where $e_i(S_h)$ = the initial tangent elastic modulus as a function of S_h under σ_3' of 1 MPa, or $E_i(S_h, 1)$. When S_h = 0%, the n and e_i in Equation (11) for sand specimens formed by Toyoura sand, No. 7 silica sand and No. 8 silica sand are respectively estimated by the least-squares regression:

$$n = \begin{cases} 0.608 \text{ (for Toyoura sand)} \\ 0.466 \text{ (for No. 7 silica sand)} \\ 0.356 \text{ (for No. 8 silica sand)} \end{cases} \tag{12}$$

$$e_{i0} = \begin{cases} 398 \text{ MPa (for Toyoura sand)} \\ 344 \text{ MPa (for No. 7 silica sand)} \\ 241 \text{ MPa (for No. 8 silica sand)} \end{cases} \tag{13}$$

where e_{i0} = e_i for a sand specimen (S_h = 0%).

Figure 8. Initial tangent modulus E_i *versus* methane hydrate saturation S_h for specimens formed by (**a**) Toyoura sand; (**b**) No.7 silica sand and (**c**) No.8 silica sand. The curves are calculated using Equation (11).
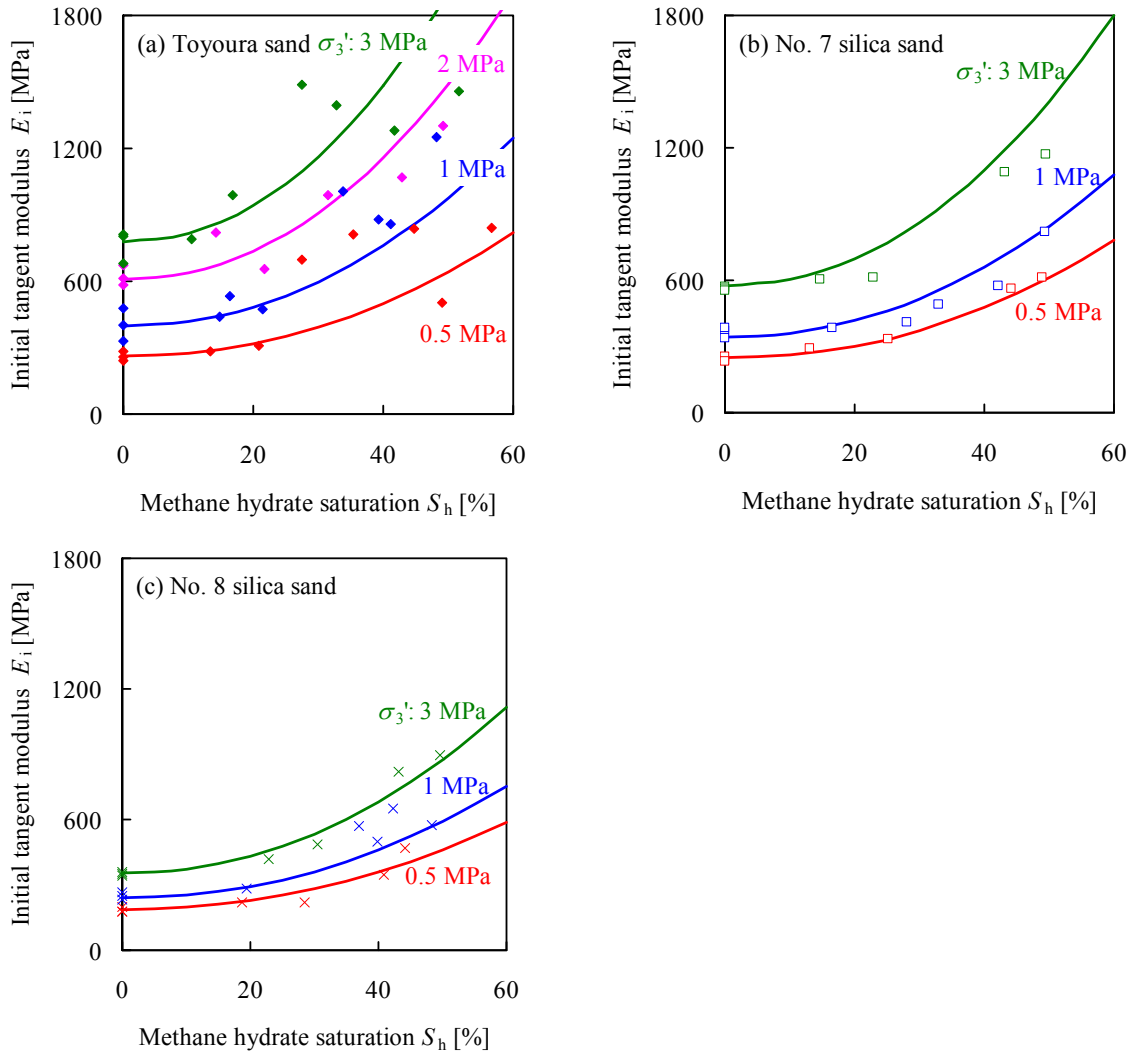

Figure 9 shows the normalized initial tangent elastic modulus $E_i*(S_h)$, or the initial tangent modulus divided by $(e_{i0} \cdot \sigma_3'^n)$, plotted against S_h for the hydrate-sand specimens:

$$E_i * (S_h) = \frac{E_i(S_h, \sigma_3')}{e_{i0} \cdot \sigma_3'^n} = \frac{e_i(S_h) \cdot \sigma_3'^n}{e_{i0} \cdot \sigma_3'^n} = \frac{e_i(S_h)}{e_{i0}} \quad (14)$$

Equation (14) is derived from Equation (11) and indicates that the relationship between E_i* and S_h is independent of σ_3'. Because e_{i0} is equal to e_i for a sand specimen, E_i* should be 1 at $S_h = 0\%$. In this study, it is assumed that the increase of E_i* is proportional to S_h to the δ-th power:

$$E_i * (S_h) = \frac{e_i(S_h)}{e_{i0}} = 1 + \gamma \cdot S_h^{\delta} \quad (15)$$

where γ and δ are estimated by the least-squares regression for the E_i*-S_h shown in Figure 9 as:

$$\gamma = 3.90 \times 10^{-4} \quad (16)$$

$$\delta = 2.10 \tag{17}$$

Because a wide variation is seen in Figure 9, there are various possible expressions for the $E_i^* - S_h$ relationship other than Equation (15).

Figure 9. Normalized initial tangent elastic modulus E_i^* *versus* methane hydrate saturation S_h for hydrate-sand specimens. The curve is calculated using Equation (15).
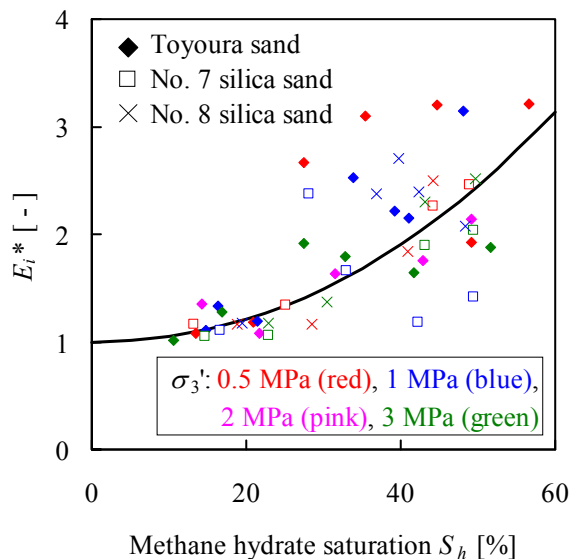
The parameter a in Equation (1), or the inverse of E_i, is given by Equations (11–17). The initial tangent modulus E_i calculated using Equations (11–17) is shown in Figure 8.

3.4. Failure Ratio

Duncan and Chang [21] defined the failure ratio R_f as:

$$R_f = \frac{q_f}{q_{ult}} \tag{18}$$

Strength q_f can be obtained from each test result as shown in Figure 7. Asymptotic value of the deviator stress q_{ult}, which is equal to the reciprocal of b as expressed by Equation (3), also can be obtained from each test result, because b can be determined by the linear approximation of the experimental (ε_a/q)-ε_a data as seen in Equation (4). Thus R_f, which is the ratio of the strength q_f to q_{ult}, is obtained from each experimental data. Figure 10 shows R_f plotted against S_h. Because the dependence of R_f on σ_3' is not clear as well as a number of different soils, we assume that R_f is independent of σ_3'. R_f shows a weak decrease with increasing S_h. However, for simplicity, we assume that R_f is independent of S_h:

$$R_f = 0.82 \tag{19}$$

which is the average R_f for the sand and hydrate-sand specimens. The data presented in Figure 10 is insufficient to determine the function form expressing the reduction in R_f to S_h. The data for S_h of higher than 60% is necessary to formulate R_f more accurately.

Figure 10. Failure ratio R_f *versus* methane hydrate saturation S_h.
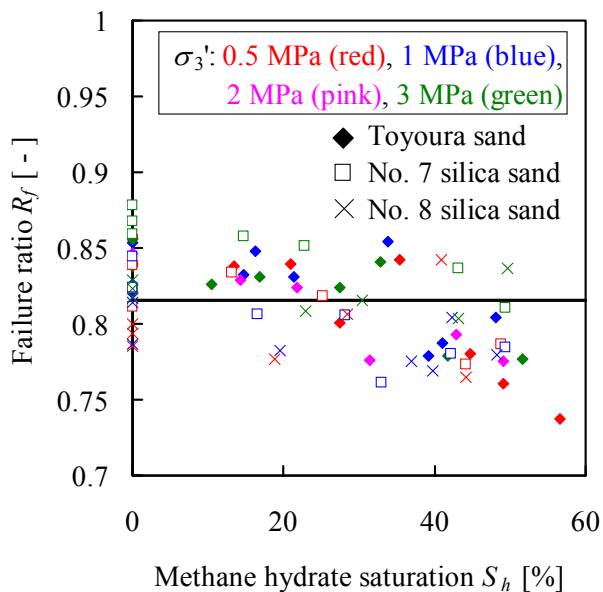
Eventually, the Duncan-Chang model (Equation (1)) may be applicable to the determination of the q-ε_a relationship of the hydrate-sand specimens using Equations (2–3, 5–9 and 11–19).

It can be conveniently used in incremental stress analysis, because the tangent elastic modulus E_t corresponding to any point on the q-ε_a curve is derived in the simple form:

$$E_t = \frac{\partial q}{\partial \varepsilon_a} = \left(1 - R_f \frac{q}{q_f}\right)^2 \cdot E_i \tag{20}$$

3.5. Lateral Strain

In this section, we examine the following expression for the relationship between the lateral strain ε_l and the axial strain ε_a:

$$\varepsilon_l = -f \cdot \varepsilon_a^2 - g \cdot \varepsilon_a \ (f > 0, g > 0) \tag{21}$$

where f and g are fitting parameters. The tangent Poisson's ratio υ_t and the initial tangent Poisson's ratio υ_i are expressed by:

$$\nu_t = -\frac{\partial \varepsilon_l}{\partial \varepsilon_a} = 2 \cdot f \cdot \varepsilon_a + g \tag{22}$$

$$\nu_i = -\frac{\partial \varepsilon_l}{\partial \varepsilon_a}\bigg|_{\varepsilon_a = 0} = g \tag{23}$$

Fitting prameters f and g can be adjusted using each experimental data on ε_l-ε_a by the least-squares regression. Figure 11 shows υ_i plotted against S_h. The S_h dependence of υ_i is weak, while the σ_3' dependence of υ_i is considerably apparent. Thus, we assume that υ_i is independent of S_h. Kulhawy and Duncan [23] described that υ_i generally decreases with increasing σ_3' in the form:

$$v_i = G - F \cdot \log\left(\frac{\sigma_3{}'}{p_a}\right) \tag{24}$$

where $G = v_i$ at 1 atm and F = the rate of change of v_i with $\sigma_3{}'$. We decided to apply a similar concept to Equation (24) to the dependence of v_i on $\sigma_3{}'$ as follows:

$$v_i\,(\sigma_3{}') = v_{i1} - m \cdot \log(\sigma_3{}') \tag{25}$$

where v_{i1} = the initial tangent Poisson's ratio v_i under $\sigma_3{}'$ of 1 MPa; and m = the coefficient determining the rate of decrease in v_i with increasing $\log(\sigma_3{}')$. The least-square logarithmic regression of experimental data gives the values of v_{i1} and m for the sand and hydrate-sand specimens:

$$v_{i1} = \begin{cases} 0.394 \text{ (for Toyoura sand)} \\ 0.324 \text{ (for No. 7 silica sand)} \\ 0.253 \text{ (for No. 8 silica sand)} \end{cases} \tag{26}$$

$$m = \begin{cases} 0.253 \text{ (for Toyoura sand)} \\ 0.245 \text{ (for No. 7 silica sand)} \\ 0.257 \text{ (for No. 8 silica sand)} \end{cases} \tag{27}$$

Figure 12 shows f plotted against v_i. Although some variation can be seen in Figure 12, f appears to be approximately proportional to v_i as:

$$f = l \times v_i \tag{28}$$

where l = the proportional constant corresponding to the slope of the line shown in Figure 12:

$$l = 0.186 \tag{29}$$

Using Equation (28), Equations (21) and (22) can be rewritten as:

$$\varepsilon_l\,(\sigma_3{}') = -(l \cdot \varepsilon_a{}^2 + \varepsilon_a) \cdot v_i\,(\sigma_3{}') \tag{30}$$

$$v_t\,(\sigma_3{}') = (2 \cdot l \cdot \varepsilon_a + 1) \cdot v_i\,(\sigma_3{}') \tag{31}$$

3.6. Calculated Deviator Stress versus Axial and Lateral Strain

The calculated q-ε_a, q-ε_l and ε_l-ε_a curves for the sand specimens (a: $S_h = 0\%$) and hydrate-sand specimens (b: $S_h = 30\%$, c: $S_h = 43\%$) under effective confining pressures $\sigma_3{}'$ of 0.5 MPa, 1 MPa, 2 MPa and 3 MPa using Equations (1) and (21) are shown in Figures 1–6. It is found that the experimental q-ε_a, q-ε_l and ε_l-ε_a curves are reasonably reproduced by Equations (1) and (21).

Figure 11. Initial tangent Poisson's ratio v_i *versus* methane hydrate saturation S_h for specimens formed by (**a**) Toyoura sand; (**b**) No.7 silica sand and (**c**) No.8 silica sand.
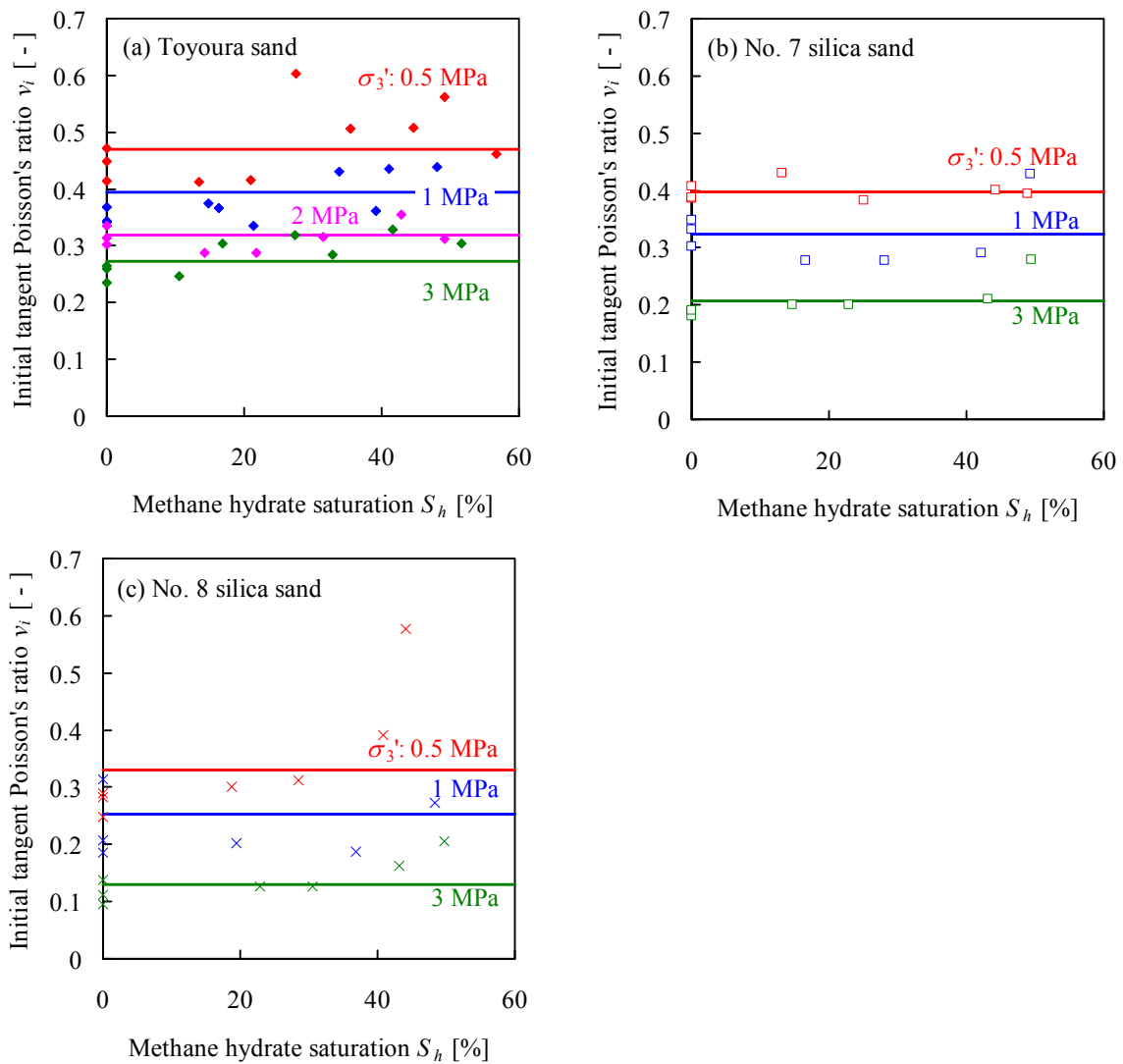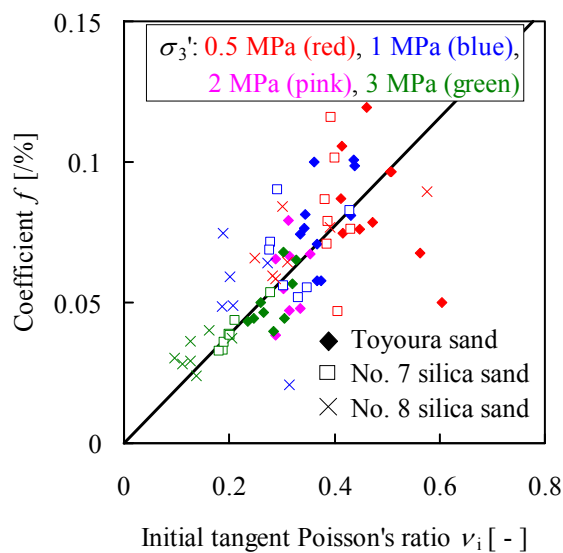

Figure 12. Coefficient *f versus* initial tangent Poisson's ratio v_i. The solid line is calculated using Equation (28).

3.7. Unloading Modulus

The unloading modulus E_{ur} is often 2 to 3 times larger than the initial tangent modulus E_i for many geomaterials [21]. Miyazaki *et al.* [16] conducted unloading-reloading test on hydrate-sand specimen formed by Toyoura sand under 1 MPa effective confining pressure to obtain E_{ur}. Figure 13 shows the E_{ur} and E_i under 1 MPa effective confining pressure plotted against methane hydrate saturation S_h. The solid line denotes the calculated e_i using Equations (13) and (15–17) for Toyoura sand specimen and the broken lines denote k-times the calculated e_i. It is found that the E_{ur} of hydrate-sand specimen is approximately 3 to 3.5 times E_i under 1 MPa effective confining pressure.

Figure 13. Unloading modulus E_{ur} and initial tangent modulus E_i *versus* methane hydrate saturation S_h for specimens formed by Toyoura sand under 1 MPa effective confining pressure. The solid line denotes e_i calculated using Equations (13) and (15–17). The broken lines are k-times the calculated e_i.
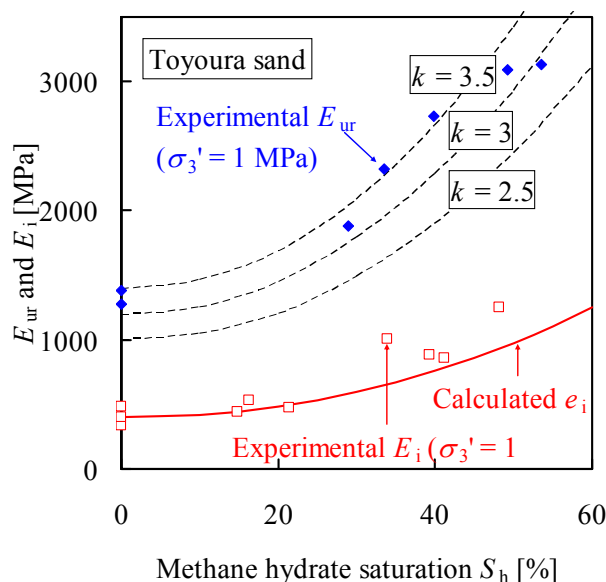
4. Conclusions

In this study, a nonlinear elastic model of the mechanical behavior of artificial methane-hydrate-bearing sediment samples was developed. The presented model is based on the Duncan-Chang model and considered the dependences of the mechanical properties on methane hydrate saturation and effective confining pressure on the basis of the experimental results reported in an earlier work [19]. Some parameters were decided depending on the type of sand forming a specimen. In addition, the plot of lateral strain *versus* axial strain was also formulated as a function of effective confining pressure. Volumetric strain has not been discussed in this paper. It may be possible to associate the volumetric strain calculated using the presented model with the volumetric strain measured in the experiments.

The presented model is very easy to introduce into finite element codes. The applicable range of the presented model will be validated by numerical simulations for the laboratory-scale methane hydrate dissociation experiments.

Acknowledgments

References

1. Makogon, Y.F. *Hydrates of Natural Gas*; Pennwell Publishing Co.: Tulsa, OK, USA, 1981.
2. Makogon, Y.F. Perspectives for the Development of Gas-Hydrate Deposits. In *Proceedings of the 4th Canadian Permafrost Conference*, Calgary, Canada, 1982; pp. 299–304.
3. Kvenvolden, K.A. A Major Reservoir of Carbon in the Shallow Geosphere? *Chem. Geol.* **1988**, *71*, 41–51.
4. Kvenvolden, K.A.; Ginsburg, G.D.; Soloviev, V.A. Worldwide Distribution of Subaquatic Gas Hydrates. *Geo-Marine Lett.* **1993**, *13*, 32–40.
5. Collett, T.S.; Dallimore, S.R. Detailed Analysis of Gas Hydrate Induced Drilling and Production Hazards. In *Proceedings of the 4th International Conference on Gas Hydrates*, Yokohama, Japan, 2002; pp. 47–52.
6. Bugge, T.; Belderson, R.H.; Kenyon, N.H. The Storegga Slide. *Phil. Trans. Royal Soc. A* **1988**, *325*, 357–388.
7. Kleinberg, R.L. Mechanical Stability of Seafloor Sediments with Application to Gas Hydrate Deposits. In *Proceedings of the 5th International Conference on Gas Hydrates*, Trondheim, Norway, 2005; pp. 736–748.
8. Sakamoto, Y.; Shimokawara, M.; Ohga, K.; Miyazaki, K.; Tenma, N.; Komai, T.; Aoki, K.; Yamaguchi, T. Field Scale Simulation for Consolidation and Gas Production Behavior during Depressurization Process of Methane Hydrate in Marine Sediments. In *Proceedings of the 2008 Offshore Technology Conference*, Houston, TX, USA, 2008; OTC19283.
9. Klar, A.; Soga, K.; Ng, M.Y.A. Coupled Deformation-Flow Analysis for Methane Hydrate Extraction. *Geotechnique* **2010**, *60*, 765–776.
10. Winters, W.J.; Pecher, I.A.; Booth, J.S.; Mason, D.H.; Relle, M.K.; Dillon, W.P. Properties of Samples Containing Natural Gas Hydrate from the JAPEX/JNOC/GSC Mallik 2L-38 Gas Hydrate Research Well, Determined using Gas Hydrate and Sediment Test Laboratory Instrument (GHASTLI). *Bull. Geol. Sur. Can.* **1999**, *544*, 241–250.
11. Winters, W.J.; Waite, W.F.; Mason, D.H.; Kumar, P. Physical Properties of Repressurized Samples Recovered during the National Gas Hydrate Program Expedition Offshore India. In *Proceedings of the 6th International Conference on Gas Hydrates*, Vancouver, Canada, 2008.
12. Masui, A.; Miyazaki, K.; Haneda, H.; Ogata, Y.; Aoki, K. Mechanical Characteristics of Natural and Artificial Gas Hydrate Bearing Sediments. In *Proceedings of the 6th International Conference on Gas Hydrates*, Vancouver, Canada, 2008.

13. Winters, W.J.; Waite, W.F.; Mason, D.H.; Gilbert, L.Y.; Pecher, I.A. Effect of Grain Size and Pore Pressure on Acoustic and Strength Behavior of Sediments Containing Methane Gas Hydrate. In *Proceedings of the 5th International Conference on Gas Hydrates*, Trondheim, Norway, 2005; pp. 507–516.

14. Masui, A.; Haneda, H.; Ogata, Y.; Aoki, K. Effects of Methane Hydrate Formation on Shear Strength of Synthetic Methane Hydrate Sediments. In *Proceedings of the 15th International Offshore and Polar Engineering Conference*, Seoul, Korea, 2005; pp. 364–369.

15. Hyodo, M.; Nakata, Y.; Yoshimoto, N.; Ebinuma, T. Basic Research on the Mechanical Behavior of Methane Hydrate-Sediments Mixture. *Soils Found.* **2005**, *45*, 75–85.

16. Miyazaki, K.; Masui, A.; Tenma, N.; Ogata, Y.; Aoki, K.; Yamaguchi, T.; Sakamoto, Y. Study on Mechanical Behavior for Methane Hydrate Sediment Based on Constant Strain-Rate Test and Unloading-Reloading Test Under Triaxial Compression. *Int. J. Offshore Polar Eng.* **2010**, *20*, 61–67.

17. Miyazaki, K.; Masui, A.; Aoki, K.; Sakamoto, Y.; Yamaguchi, T.; Okubo, S. Strain-Rate Dependence of Triaxial Compressive Strength of Artificial Methane-Hydrate-Bearing Sediment. *Int. J. Offshore Polar Eng.* **2010**, *20*, 256–264.

18. Miyazaki, K.; Masui, A.; Sakamoto, Y.; Tenma, N.; Yamaguchi, T. Effect of Confining Pressure on Triaxial Compressive Properties of Artificial Methane Hydrate Bearing Sediments. In *Proceedings of the 2010 Offshore Technology Conference*, Houston, TX, USA, 2010; OTC20721.

19. Miyazaki, K.; Masui, A.; Sakamoto, Y.; Aoki, K.; Tenma, N.; Yamaguchi, T. Triaxial Compressive Properties of Artificial Methane-Hydrate-Bearing Sediment. *J. Geophys. Res.* **2011**, *116*, B06102.

20. Miyazaki, K.; Aoki, K.; Tenma, N.; Sakamoto, Y.; Yamaguchi, T. Application of Nonlinear Elastic Constitutive Model to Analysis of Artificial Methane-Hydrate-Bearing Sediment Sample. In *Proceedings of the 9th ISOPE Ocean Mining Symposium*, Maui, HA, USA, 2011; pp. 15–20.

21. Duncan, J.M.; Chang, C.Y. Nonlinear Analysis of Stress and Strain in Soils. *J. Soil Mech. Found. Div.* **1970**, *96*, 1629–1653.

22. Janbu, N. Soil Compressibility as Determined by Oedometer and Triaxial Test. In *Proceedings of the 3rd European Conference on Soil Mechanics and Foundation Engineering*, Wiesbaden, Germany, 1963; pp. 19–25.

23. Kulhawy, F.H.; Duncan, J.M. Stresses and Movements in Oroville Dam. *J. Soil Mech. Found. Div.* **1972**, *98*, 653–665.